JOURNAL OF SOLID STATE CHEMISTRY **140,** 7–13 (1998)
ARTICLE NO. SC987674

Structure and Magnetism in $CrTa_2O_6$: A Trirutile Oxide Based on Cr^{2+}

M. Saes, N. P. Raju, and J. E. Greedan[1]

Department of Chemistry and Brockhouse Institute for Materials Research, McMaster University, Hamilton, Canada L8S 4M1

Received June 30, 1997; in revised form October 21, 1997; accepted October 21, 1997

$CrTa_2O_6$, a rare example of an oxide containing Cr^{2+}, was prepared by solid state reaction from a mixture of Cr_2O_3, Ta_2O_5, and Ta in a sealed silica tube at 1050°C. It exhibits a slightly distorted trirutile structure described in $P2_1/n$ with $a = 4.738(1)$, $b = 4.7421(6)$, $c = 9.2972(9)$, and $\beta = 90°55'(1)$ as determined from Guinier–Hagg data and Cu$K\alpha_1$ radiation, in excellent agreement with previous reports. The crystal structure was refined from powder neutron diffraction data at 20 K. The Cr^{2+} environment is distorted from that usually found in trirutile oxides with Cr–O distances ranging from 2.06(1) to 2.270(9) Å consistent with a static Jahn–Teller distortion as expected for high-spin Cr^{2+}. Magnetic susceptibility data show a Curie–Weiss behavior with $C = 2.79(1)$ emu mol^{-1} K^{-1}, which compares well with the expected value of 3.0 emu mol^{-1} K^{-1} for the high-spin state. A $\theta_c = -30.0(8)$ K indicates the dominance of antiferromagnetic exchange. A susceptibility maximum at 11 K is evidence for long-range antiferromagnetic order. Low-temperature neutron diffraction data confirm a $T_N = 10.3(1)$ K and a complex magnetic structure with ordering wave vector $\vec{k} = (1/4\ 1/4\ 1/4)$ as seen for some other trirutile oxides. For $T > T_N$, two-dimensional, short-range correlations are seen in the form of a Warren line shape. Interestingly, the two-dimensional correlations persist into the ordered regime, at least to 9.0 K. The properties of $CrTa_2O_6$ are compared with other known trirutile MTa_2O_6 and MSb_2O_6 materials. © 1998 Academic Press

INTRODUCTION

Oxides with the trirutile structure of composition $M^{2+}B_2^{5+}O_6$ exist for various combinations of divalent pentavalent ions, for example, M = V, Cr, V, Fe, Co, and Ni for B = Ta and M = Co, Ni, and Cu for B = Sb (1–11). All crystallize in $P4_2/mnm$ or $P2_1/n$, when M is a Jahn–Teller species such as Cr^{2+} or Cu^{2+}. The crystallographic ordering between M and B, Fig. 1, results in a M sublattice of $I4/mmm$ symmetry, the same as that found for the magnetic sublattice of K_2NiF_4 structure materials, which are considered to be among the best examples of two-dimensional antiferromagnets (12). The two dimensionality arises due to a combination of factors including a more convoluted interlayer exchange pathway and also a symmetry cancellation effect between antiferromagnetically coupled square planar layers at $z = 0$ and $z = 1/2$, which can be regarded as a form of geometric frustration. The ligand positions within the square planar layers, Fig. 2, allow 180° M–O–M superexchange between nearest neighbors (nn) and thus a large, negative J_{nn} results and the condition $J_{nn} \gg J_{nnn}$ applies. In addition, $J_{nn}^{intra} \gg J^{inter}$ due to the aforementioned frustration. The above relationships result in a set of magnetic properties for K_2NiF_4 materials characterized by extensive short-range, two-dimensional correlations followed by a crossover to three-dimensional, long-range order.

For the MB_2O_6 trirutiles, in contrast, intraplanar ligand positions, also shown in Fig. 2, do not favor a dominant J_{nn}. Rather, $J_{nnn} > J_{nn}$ is more likely due to the long bond distances and large bond angles involved in J_{nn} while a favorable 180° M–O–O–M pathway is available for J_{nnn}. Note also that the two possible J_{nnn} pathways are not equivalent, which suggests the possibility of one-dimensional, short-range correlations. Two dimensionality is expected for $J_{nn} \approx J_{nnn}$. It is noteworthy that for this condition a form of intraplanar magnetic frustration will result as illustrated in Fig. 3.

Evidence for short-range magnetic correlations in the MB_2O_6 materials is clear from the presence of broad susceptibility maxima at temperatures significantly higher than the critical temperature for three-dimensional order, T_N. In fact, a measure of the importance of short-range correlations in these materials is afforded by the ratio, $T(\chi_{max})/T_N$, and values for the MB_2O_6 group are collected in Table 1. A wide variation is seen from large ratios for $NiSb_2O_6$ and $CuSb_2O_6$ to much smaller values for VTa_2O_6 and $FeTa_2O_6$. A detailed analysis of susceptibility data indicates one-dimensional, short-range order (SRO) for the Ni and Cu antimonates with J/k values of −41 K and −43 K, respectively (8, 11). For the Cu material, $J^{inter}/J^{intra} = 10^{-3}$, supporting the linear chain model. On the other hand, $CoTa_2O_6$ has been analyzed in terms of square planar SRO with $J_{nnn}/J_{nn} = 60$ (6). In the long-range ordered state, two magnetic structures are found with propagation vectors,

[1] To whom correspondence should be addressed.

0022-4596/98 $25.00

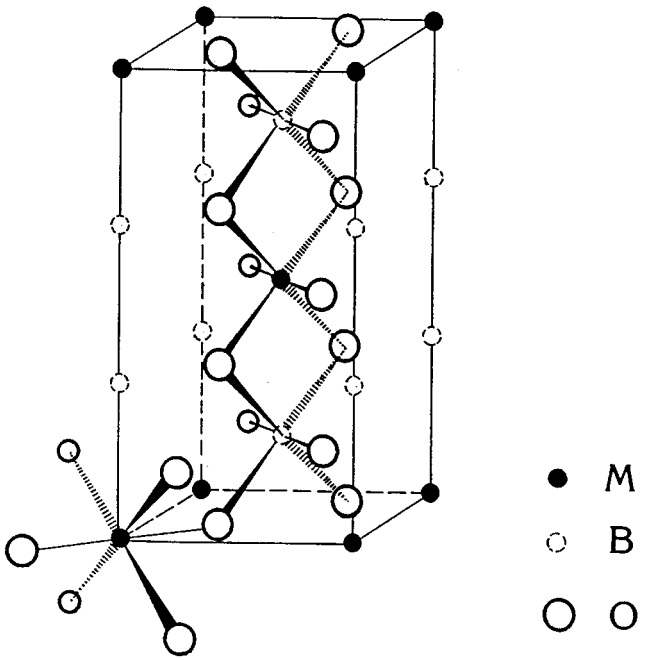

FIG. 1. The trirutile structure, MB_2O_6.

$\hat{k} = (1/2\ 0\ 1/2)$ and $\hat{k} = (1/4\ 1/4\ 1/4)$, which are significantly more complex than that usually found for the K_2NiF_4 materials (6). The $\hat{k} = (1/4\ 1/4\ 1/4)$ structure is remarkable as the nn spins flip by 90° along all three dimensions upon translation. Both structures are found for the tantalates but only the $\hat{k} = (1/2\ 0\ 1/2)$ structure occurs for the antimonates as seen from Table 1.

Among the known MB_2O_6 trirutiles, $CrTa_2O_6$ has been studied in less detail than the others, for example, the T_N and magnetic structure are unreported. Additionally, this material represents a rare, possibly unique, example of the Jahn–Teller Cr^{2+} ion in an oxide environment.

EXPERIMENTAL

Preparation

The synthesis of $CrTa_2O_6$ was achieved with a few modifications of the procedure described previously (3). Stoichiometric amounts of Cr_2O_3, Ta_2O_5 (CERAC, 99.99%), and Ta(AESAR, 99.98%) were mixed in stoichiometric amounts in accord with

$$5Cr_2O_3 + 9Ta_2O_5 + 2Ta = 10CrTa_2O_6. \qquad [1]$$

The intimately ground mixture was fixed in a sealed, evacuated silica tube at 1050°C for 48 hours. The Cr_2O_3 was prepared by decomposing CrO_3 (BDH Chemicals 99.99%) at 500°C in air. The product is a black powder.

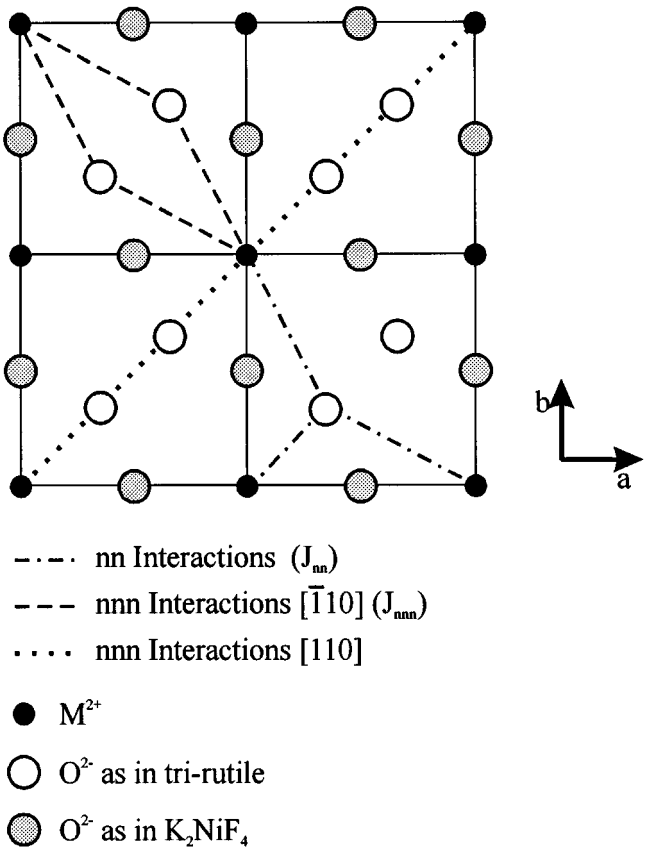

FIG. 2. The $z = 0$ layer in both the K_2NiF_4 and trirutile structures, showing the transition metal and oxide positions and the potential super exchange pathways connecting nn and nnn.

X-Ray Powder Diffraction

Powder diffraction patterns were obtained using a Guinier–Hagg camera (IRDAB XDC700), monochromated Cu$K\alpha_1$ radiation ($\lambda = 1.54056$ Å) and an internal Si standard. The films were read with a LS-20 computer automated line scanner (KEJ Instruments, Taby Sweden). Unit cell parameters were determined using the program LSUDF.

Magnetic Susceptibility

A SQUID magnetometer was employed to measure magnetic susceptibilities in the range 5 to 350 K in an applied field of 100G. Both field cooled (100G) and zero-field cooled (0.5G) data were collected.

Thermal Analysis

The weight gain upon air oxidation was followed with a Netzsch STA 409 Thermal Analyzer. The sample was heated to 1200°C at a rate of 10°C/min in flowing air.

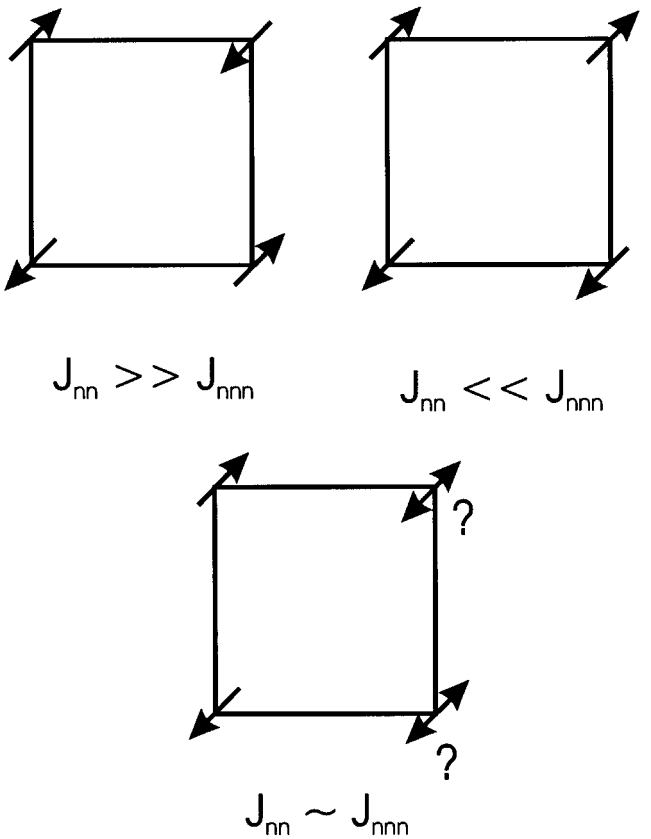

FIG. 3. Frustration arising in the square planar lattice for the condition $|J_{nn}| \approx |J_{nnn}|$.

Neutron Powder Diffraction

Powder neutron diffraction data were obtained on the DUALSPEC diffractometer at the Chalk River laboratories of AECL. Neutron wavelengths of 2.3746 and 1.3297 Å were used. The temperature range was 5 to 20 K and the sample was cooled in a liquid helium cryostat and contained in a vanadium tube sealed with an indium wire gasket. Data were refined using the Reitveld code FULLPROF (16).

TABLE 1
Selected Magnetic Data for the MB_2O_6 Trirutile Oxides

	$T(\chi_{max})$ (K)	T_N (K)	$T(\chi_{max})/T_N$	$\hat{k}$	Reference
VTa_2O_6	26(2)	21(1)	1.2	(1/2 0 1/2)	2
$CrTa_2O_6$	—	—	—	—	—
$FeTa_2O_6$	15(1)	8.1(1)	1.7	(1/2 0 1/2)	13
$CoTa_2O_6$	15.6(2)	6.63(5)	2.3	(1/4 1/4 1/4)	6
$NiTa_2O_6$	25(1)	10.3(1)	2.4	(1/4 1/4 1/4)	2
$CoSb_2O_6$	35	13.0(2)	2.7	(1/2 0 1/2)	6
$NiSb_2O_6$	36	2.5	14.4	(1/2 0 1/2)	8
$CuSb_2O_6$	60	9(1)	6.7	(1/2 0 1/2)	11, 14

RESULTS AND DISCUSSION

General Characterization

The X-ray diffraction pattern of the black powder prepared by solid state reaction was clearly of the trirutile type by visual inspection. It is well known that an extensive solid solution exists between the normal rutile, $CrTaO_4$, which contains only Cr^{3+} and $CrTa_2O_6$ and that the trirutile supercell persists up to 17% Cr^{3+} (3). Thus, it is important to obtain accurate unit cell constants and to determine, analytically, the Cr^{2+} content

Unit cell constants determined from the Guinier data are $a = 4.738(1)$, $b = 4.7421(6)$, $c = 9.2972(9)$ Å, and $\beta = 90°55'(1)$; these are in good agreement with previous results for the $CrTa_2O_6$ end member, but the present values are more precise (3).

The weight gain upon air oxidation was found to be 1.54%, which is in excellent agreement with the expected value of 1.57%, which places an upper limit of 3% for the Cr^{3+} content.

Crystal Structure

Although a detailed structure was proposed some time ago from x-ray powder diffraction data, a least-squares refinement was not carried out (3). Thus, the crystal structure was redetermined from a conventional Rietveld refinement of powder neutron data obtained at 20 K with $\lambda = 1.3297$ Å as shown in Fig. 4. The refinement proceeded smoothly in $P2_1/n$ using the results for $CuSb_2O_6$ as starting parameters (11), and the values obtained are collected in

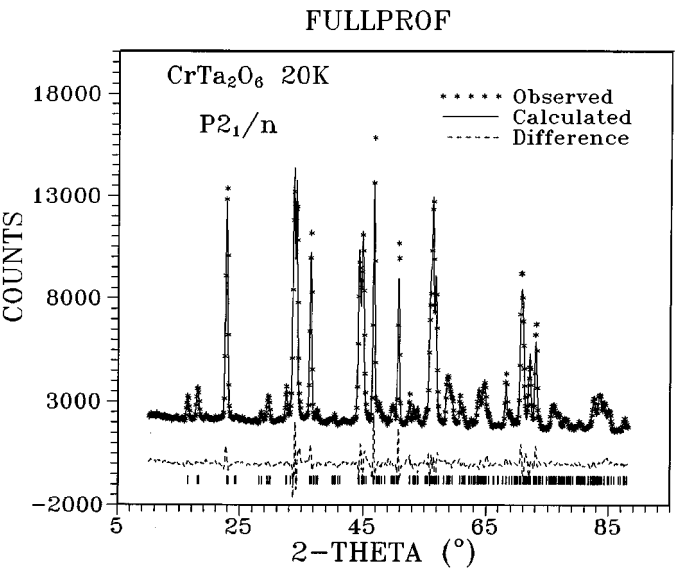

FIG. 4. A Rietveld analysis of the crystal structure of $CrTa_2O_6$ at 20 K.

TABLE 2
Rietveld Refinement Details for $CrTa_2O_6$ at 20 K

Wavelegth (Å)	1.3297
a (Å)	4.7381(7)
b (Å)	4.7413(7)
c (Å)	9.297(1)
β (°)	91.050(6)

Positional and thermal parameters

	x	y	z	B (Å^2)
Ta	0.0046(23)	0.0129(23)	0.3343(9)	0.50(17)
O1	0.3038(31)	0.3124(23)	− 0.0042(12)	0.48(17)
O2	0.3016(26)	0.3110(22)	0.3258(10)	0.33(17)
O3	− 0.2976(18)	− 0.2765(23)	0.3122(8)	0.62(20)

Note: Space group $P2_1/n$. No. (*hkl*) 242; No. profile points 800. R_p 0.048; R_{wp} 0.064; R_B 0.049; R_E 0.020. Definitions of R's: $R_p = 100 \times \sum|Y_{OBS} - Y_{CALC}|/\sum Y_{OBS}$; $R_{wp} = 100 \times \{[\sum_w(Y_{OBS} - Y_{CALC})^2]/[\sum_w(Y_{OBS})^2]\}^{1/2}$; $R_B = 100 \times \sum|I_{OBS} - I_{CALC}|/\sum I_{OBS}$; $R_E = \{(N-P)/\sum_w(Y_{OBS})^2\}^{1/2}$.

Table 2. Selected bond distances and angles appear in Table 3. Examination of the bond distances discloses a highly distorted Cr–O environment. The extent of this distortion is appreciated upon comparison with corresponding distances for the M–O octahedral environment in the known MB_2O_6 compounds, Table 4. It is clear that $CrTa_2O_6$ shows the largest M-site distortion index of any of the trirutiles, which is consistent with a static Jahn–Teller distortion as expected for a high-spin Cr^{2+} ion.

TABLE 3
Selected Bond Distances (Å) and Angles (°)

Cr–O1	2.066(13)	2×	Ta–O1	2.042(15)
Cr–O2	2.062(10)	2×	Ta–O1	1.974(15)
Cr–03	2.270(9)	2×	Ta–O2	997(16)
			Ta–O2	2.006(14)
			Ta–O3	1.991(15)
			Ta–O3	1.940(13)
O1–Cr–O1	180.0		O1–Ta–O1	79.7(6)
O1–Cr–O2	88.9(5)		O1–Ta–O2	93.2(6)
O1–Cr–O3	89.1(4)		O1–Ta–O2	98.6(7)
O1–Cr–O3	90.9(4)		O1–Ta–O3	93.9(6)
O1–Cr–O2	91.1(5)		O1–Ta–O3	173.9(7)
O2–Cr–O3	78.0(4)		O1–Ta–O2	94.9(6)
O2–Cr–O3	102.0(4)		O1–Ta–O2	176.3(8)
O2–Cr–O2	180.0		O1–Ta–O3	90.7(6)
O3–Cr–O3	180.0		O1–Ta–O3	94.2(6)
			O2–Ta–O2	88.6(6)
			O2–Ta–O3	171.7(6)
			O2–Ta–O3	87.5(6)
			O2–Ta–O3	86.1(6)
			O2–Ta–O3	87.5(5)
			O2–Ta–O3	85.9(6)

TABLE 4
***M*–O Distances and Distortion Indices in the MB_2O_6 Trirutiles**

M	M–O1 (Å)	M–O2 (Å)	Distortion index
V	2.10(1)	2.10(1)	0.0
Cr	2.06(1)	2.270(9)	9.9
Fe	2.06(2)	2.13(1)	3.3
Co(Ta)	2.082(2)	2.101(3)	0.9
Co(Sb)	2.026(3)	2.068(3)	2.1
Ni(Ta)	2.06(2)	2.06(2)	0.0
Ni(Sb)	2.039(3)	2.040(3)	0.0
Cu	2.004(4)	2.012(4)	5.5
		2.120(4)	

Note. Distortion Index = $\{[(M\text{–}O2) - (M\text{–}O1)]/\langle M\text{–}O\rangle\} \times 100$.

Magnetic Susceptibility

Figure 5 shows the temperature dependence of the magnetic susceptibility for $CrTa_2O_6$ over the range 5 to 350 K. It is clear that the Curie–Weiss law holds down to low temperatures and the refined parameters are $C = 2.79(1)$ emu mol^{-1} K^{-1} and $\theta_c = -30.0(8)$ K. These values are also in good agreement with previous reports (3). From the Curie constant a $\mu_{eff} = 4.72$ Bohr Magnetons can be derived, which is consistent with the expected value of 4.98 B.M. for the $S = 2$ ground state of high-spin Cr^{2+}. The fairly large, negative Weiss constant indicates the dominance of antiferromagnetic exchange in this material. The inset of Fig. 5 discloses a susceptibility maximum at about 11 K, indicating the probable onset of long-range antiferromagnet order.

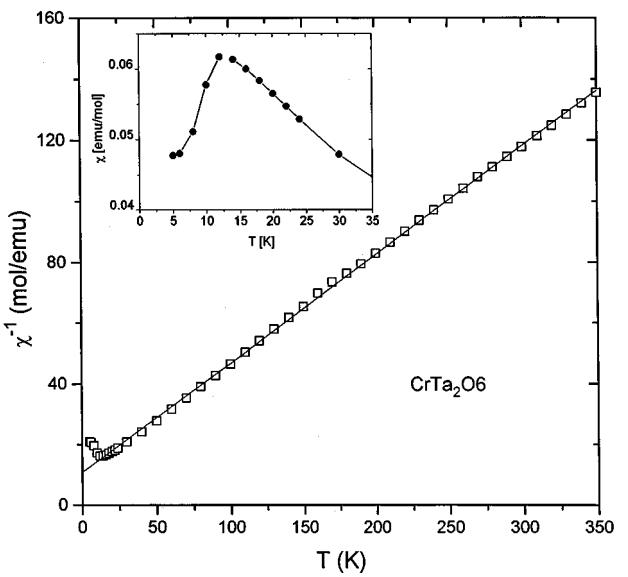

FIG. 5. Magnetic susceptibility data for $CrTa_2O_6$ in the temperature range 5 to 300 K. The inset shows data for 5 to 30 K.

Low-Temperature Neutron Diffraction

Several neutron data sets were obtained over the temperature range 5 to 20 K. Inspection indicated the presence of at least six new reflections below 11 K, the position of the susceptibility maximum. Results for selected temperatures are shown in Fig. 6. Note first that sharp Bragg peaks are evident in the 10-K data, which disappear by 10.5 K. The Bragg peaks are evidence for the onset of long-range antiferromagnetic order (AF-LRO) and the transition temperature appears to lie between 10.0 and 10.5 K.

There is also evidence of magnetic SRO from another obvious feature of Fig. 6, the broad, asymmetric maximum just above 10(°) for the data at 10.5 and 11.0 K. This shape is clearly of the Warren type, which indicates that the SRO is two dimensional (15). A fit of 10.5-K data appears in Fig. 7. The Warren type maximum persists up to at least 13.0 K (data not shown) and, interestingly, down to 9.0 K. Thus, the 2D SRO coexists with the 3D LRO over a fairly broad temperature range.

A detailed fitting of the data in the two-theta interval 9(°) to 18(°) was carried out using a convolution of a Gaussian line shape for the sharp component and a Warren line shape for the broad component over the temperature range 5 to 13 K. The temperature dependence of the extracted Bragg peak intensity is shown in Fig. 8. A simple extrapolation to zero intensity gives an estimate of 10.3(1) K for T_N. Thus, the ratio $T(\chi_{max})/T_N \approx 1.1$, the smallest value for any MB_2O_6 material in Table 1. Thus, SRO, while clearly present, plays a much smaller role in the magnetism of $CrTa_2O_6$ than in other members of the series.

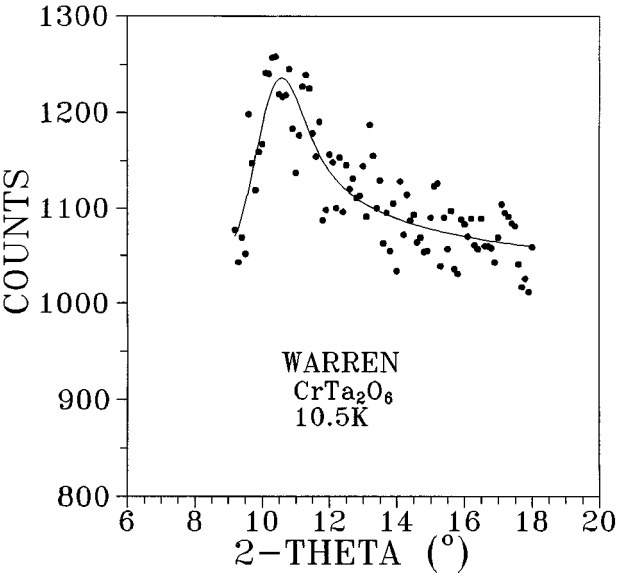

FIG. 7. A fit of the 10.5-K data to the Warren function.

From the fitting of the Warren component, an estimate of the 2D correlation length can be obtained. A value of 110(12) Å is extracted, which remains roughly constant from

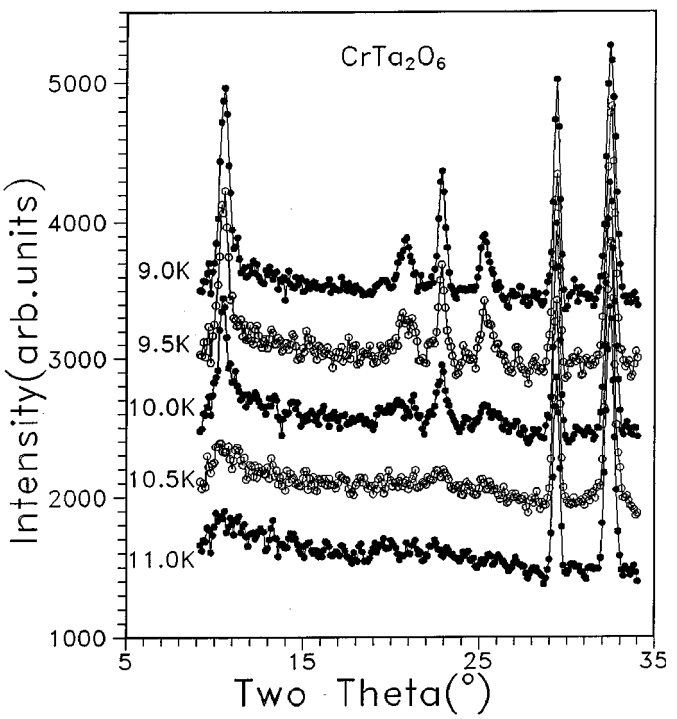

FIG. 6. Neutron diffraction data for $CrTa_2O_6$ from 9.0 to 11.0 K.

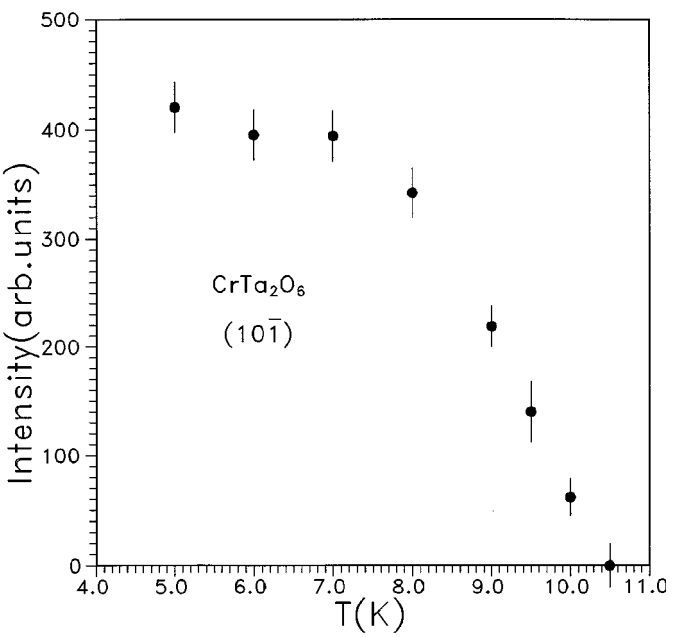

FIG. 8. Temperature dependence of the intensity of the (10$\bar{1}$) magnetic Bragg peak for $CrTa_2O_6$.

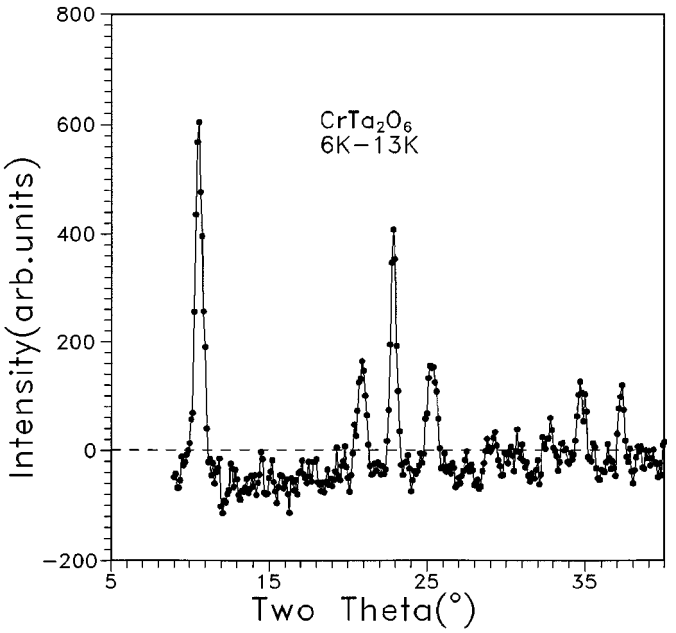

FIG. 9. The magnetic Bragg peaks for $CrTa_2O_6$ obtained by subtraction of 13-K data from 6-K data.

9.0 to 11.0 K but drops to 47(10) Å at 13.0 K. The magnetic unit cell or, alternatively, the wave vector which describes the long range order, was deduced by comparison of the positions of the clearly identifiable magnetic reflections, Fig. 9, with calculated values. The only satisfactory fit was obtained for a magnetic cell $a_{mag} = 2\sqrt{2}a$, $b_{mag} = 2\sqrt{2}b$, and $c_{mag} = 4c$ as seen in Table 5. Note that this is equivalent to a magnetic cell, $a_{mag} = 4a$, $b_{mag} = 4b$, and $c_{mag} = 4c$ by a reorientation of the axes along the *ab* diagonal of the chemical cell.

This is the same cell as found for $CoTa_2O_6$ and $NiTa_2O_6$ and is consistent with an ordering wave vector $\hat{k} =$ (1/4 1/4 1/4). An attempt to model the magnetic structure using the FULLPROF code was partially successful. In principle, there are 64 Cr moments in the magnetic unit cell and in FULLPROF only 56 magnetic sites can be accommodated. By constraining all of the spins to the *ab* plane, the number of independent moments can be reduced to 32 due to an *I*-centering. With the above constraint and a moment of 4 Bohr Magnetons per Cr^{2+}, most of the magnetic powder profile can be modeled. It is clear, however, that in order to improve the fit it will be necessary to allow some tilting out of the plane for one sublattice of spins as found previously for $CoTa_2O_6$ (6). This removes the *I*-centering and renders the calculation impossible with the existing code.

TABLE 5
Observed and Calculated Magnetic Peak Positions for $CrTa_2O_6$ on a Magnetic Cell $2(\sqrt{2})a$, $2(\sqrt{2})b$, $4c$

Peak position Observed (2θ)	Peak position Calculated (2θ)	(hkl)
10.721(7)	10.745	$10\bar{1}$
21.02(2)	21.04	105
23.038(9)	23.06	$20\bar{3}$
25.44(2)	25.46	204
34.88(4)	34.89	127
37.41(2)	37.41	$21\bar{8}$

SUMMARY

That $CrTa_2O_6$ is a rare example of an oxide based on Cr^{2+} is confirmed by crystallographic, TGA, and magnetic susceptibility studies. The compound shows long-range antiferromagnetic order below 10.3 K with a complex magnetic structure described by a magnetic unit cell 32 times the volume of the chemical cell, specifically, with $\hat{k} =$ (1/4 1/4 1/4). $CrTa_2O_6$ also exhibits 2D short-range order but the SRO regime is much less extensive than for most of the other MB_2O_6 materials studied previously. These observations suggest that the intraplanar J_{nn} and J_{nnn} are comparable in magnitude, unlike the cases of $CuSb_2O_6$ and $NiSb_2O_6$, where the SRO is clearly 1D and the condition $|J_{nn}| \gg |J_{nnn}|$ must hold, and in addition, that the interplanar exchange coupling must be relatively stronger in $CrTa_2O_6$.

The origins of the clear and sometimes striking differences in magnetic behavior among the various MB_2O_6 trirutile compounds cannot be understood at present in detail. More experimental results are needed, such as measurements of the J_{nn}/J_{nnn} ratio, and a comprehensive theory to explain the complex magnetic structures observed is lacking.

ACKNOWLEDGMENTS

We thank the Natural Sciences and Engineering Research Council of Canada for a Research grant to J. E. Greedan and a Major Facilities Access grant to the Brockhouse Institute for Materials Research. C. V. Stager provided access to the S.Q.U.I.D. magnetometer and R. Donaberger (McMaster) and I. Swainson (Steacie Institute, National Research Council of Canada) provided assistance with the neutron diffraction measurements.

REFERENCES

1. J. C. Bernier and P. Poix, *Ann. Chim.* **3,** 119 (1968).
2. S. M. Eicher, Ph.D. dissertation, McMaster University, 1984.
3. P. Massard, J. C. Bernier, and A. Michel, *Ann. Chim.* **6,** 41 (1974).
4. H. Weitzel and S. Klein, *Acta. Crystallogr. A* **30,** 380 (1974).
5. O. von Heidenstom, *Ark. Kemi* **28,** 375 (1968).
6. J. N. Reimers, J. E. Greedan, C. V. Stager and R. K. Kremer, *J. Solid State Chem.* **83,** 20 (1989).
7. J. P. Turbil and J. C. Bernier, *C.R. Acad. Sci. Paris C* **277,** 1347 (1973).

8. E. Ramos, F. Fernandez, A. Jerez, C. Pico, R. Rodriguez-Carvajal, R. Saez-Puche, and M. L. Viega, *Mat. Res. Bull.* **27,** 1041 (1992).
9. A. Bystrom, B. Hok, and B. Mason, *Ark. Kemi Mineral. Geol B* **15,** 1 (1941).
10. J. N. Reimers and J. E. Greedan, unpublished.
11. A. Nakua, J. E. Greedan, J. N. Reimers, H. Yun, and C. V. Stager, *J. Solid State Chem.* **91,** 105 (1991).
12. L. J. de Jongh and A. R. Miedema, *Adv. Phys.* **23,** 1 (1974).
13. S. M. Eicher, J. E. Greedan, and K. J. Lushington, *J. Solid State Chem.* **62,** 220 (1986).
14. A. M. Nakua and J. E. Greedan, *J. Solid State Chem.* **118,** 199 (1995).
15. B. E. Warren, *Phys. Rev.* **59,** 693 (1941).
16. J. Rodriguez-Carvajal, "FULLPROF: Abstracts of the Satellite Meeting on Powder Diffraction of the XV Congress of the International Union of Crystallography, Toulouse, 1990." p. 217.